nature portfolio

https://doi.org/10.1038/s41567-022-01557-4

Supplementary information

Broken-symmetry states at half-integer band fillings in twisted bilayer graphene

In the format provided by the authors and unedited

Broken-symmetry states at half-integer band fillings in twisted bilayer graphene

Saisab Bhowmik,[1,*] Bhaskar Ghawri,[2] Nicolas Leconte,[3] Samudrala Appalakondaiah,[3] Mrityunjay Pandey,[4] Phanibhusan S. Mahapatra,[2] Dongkyu Lee,[3,5] K. Watanabe,[6] T. Taniguchi,[7] Jeil Jung,[3,5,†] Arindam Ghosh,[2,4] and U. Chandni[1,‡]

[1] *Department of Instrumentation and Applied Physics, Indian Institute of Science, Bangalore, 560012, India*
[2] *Department of Physics, Indian Institute of Science, Bangalore, 560012, India*
[3] *Department of Physics, University of Seoul, Seoul 02504, Korea*
[4] *Centre for Nano Science and Engineering, Indian Institute of Science, Bangalore 560 012, India*
[5] *Department of Smart Cities, University of Seoul, Seoul 02504, Korea*
[6] *Research Center for Functional Materials, National Institute for Materials Science, Namiki 1-1, Tsukuba, Ibaraki 305-0044, Japan*
[7] *International Center for Materials Nanoarchitectonics, National Institute for Materials Science, Namiki 1-1, Tsukuba, Ibaraki 305-0044, Japan*

SUPPLEMENTARY INFORMATION

I. SIMULATION

Here, we outline the details of the tight-binding hopping terms, in particular the interlayer coupling that we have used in our simulations. We then show the band structures corresponding to a shifted origin 1D potential that shows the relative robustness of band folding features. We further present band structures for different Hamiltonian model parameters without and with spin-orbit coupling (SOC) terms to better understand the role of the different terms in the Hamiltonian.

A. Twisted bilayer graphene's tight-binding Hamiltonian

The twisted bilayer graphene (TBG) interlayer hopping terms between atoms at lattice points $\mathbf{R}_i$ and $\mathbf{R}_j$ are given by [1]

$$-t_{lm} = -t(\mathbf{R}_l, \mathbf{R}_m) = S_0 \exp[(\mathbf{d}\cdot\mathbf{e}_z - p)/q] \times \left[V_{pp\sigma}(d) \left(\frac{\mathbf{d}\cdot\mathbf{e}_z}{d} \right)^2 \right]. \tag{1}$$

with $\mathbf{d} = \mathbf{R}_l - \mathbf{R}_m$, $d = |\mathbf{d}|$ and $\mathbf{e}_z$ the unit vector parallel to the z axis and where [2]

$$V_{pp\sigma}(d) = V^0_{pp\sigma} \exp\left(-\frac{(d - d_0)}{r_0} \right) \tag{2}$$

with d_0 the interlayer distance, a_0 the interatomic carbon distance, $r_0 = 0.184a$ and $V^0_{pp\sigma} = -0.48$ eV is the transfer integral between two vertically aligned atoms. This form in Eq. 2 is widely used in the literature [3] and is good at reproducing the largest magic angle in TBG, even though the corresponding effective hopping term, obtained by summating intralayer intra-sublattice terms [4], of -2.45 eV (when using $V^0_{pp\pi} = 2.7$ eV for the transfer integral between nearest-neighbor atoms) corresponds to a Fermi velocity which is much smaller than experiment or even local density approximation (LDA). To correct for this approximate model in square brackets, we introduced the variables $p = 1.34$ and $q = 3.25$ to better capture the inter-layer distance modulations that enter the fitting procedure to the DFT tunneling at the K-point for all slidings as well as the magic angle renormalization factor S_0 equal to 0.895 for these structures that we relaxed using LAMMPS MD relaxations [5] using EXX-RPA-informed [6] force fields. This choice of S_0 value leads to the maximum flatness of bands at 1.08° when all terms but the first are equal to zero in the Hamiltonian from Eq. (2) in the manuscript. For the intralayer terms we simply use the F2G2 model [4].

B. Doubling of the bands due to band-folding

In Fig. S1, we illustrate how the existence of a potential that doubles the initial TBG moiré period by a factor two effectively leads to band-folding and associated doubling of the initial 4-fold degenerate valence and conduction bands. We calculate the band structures in the smallest moire triangular unit cell and compare with the folded bands with twice the original unit cell area where we can observe how the initial bands are being doubled in number. We neglect any spin/valley degeneracy lifting terms in the Hamiltonian and will discuss their effect further in Sect. I D.

* saisabb@iisc.ac.in
† jeiljung@uos.ac.kr
‡ chandniu@iisc.ac.in

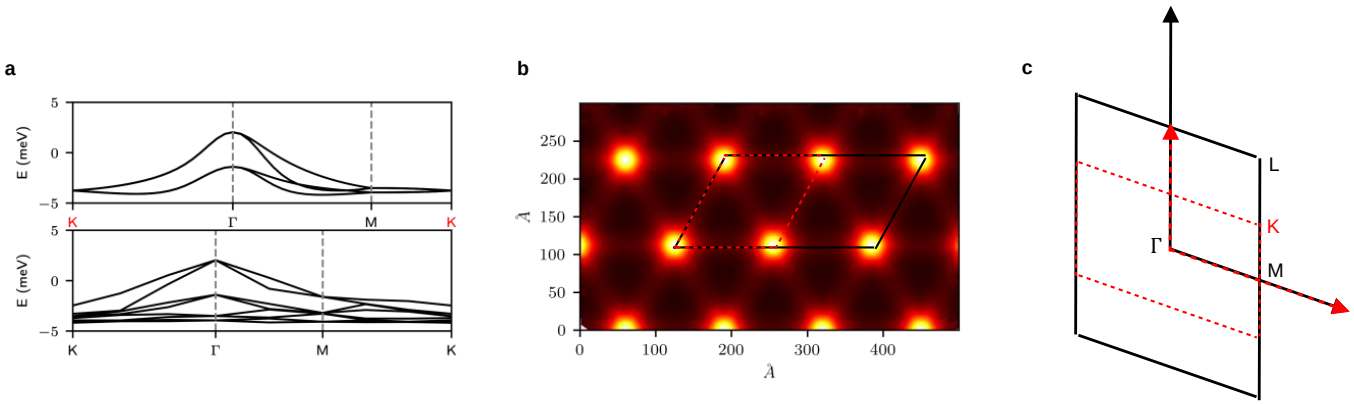

Supplementary Fig. S1. **Band folding and doubling of bands**. **a.** The top panel illustrates the bandstructure for the unperturbed original triangular moiré cell illustrated by the parallelogram linking 4 closest AA-stacking bright dots in **b.**, whereas the bottom panel shows the band structure for the doubled area supercell. The spin is neglected in this figure, as such we see a total of 4 bands (two valleys for the conduction band and valence band) in the top panel becoming 8 bands by band-folding in the bottom panel. **b.** Real-space schematic of the single and double area supercells indicated by the dashed red and black solid parallelograms. **c**. The associated BZ for the band structures for the single and double area supercells indicated also with dashed red and black solid lines.

C. Alternative 1D potential modulation

We have chosen a specific form of the 1D sine potentials in the main text to obtain the folded bands in the larger period cell. Here, we provide an additional 1D potential that leads to a doubled supercell area compared to the moiré pattern unit cell area that leads to quantitatively different types of folded bands. In Fig. S2, we apply a cosine instead of a sine 1D modulation in Eq. 2 in the manuscript (set $\phi = \pi/2$). In this case, the AA stacking regions are located where the 1D potential is maximal or minimal.

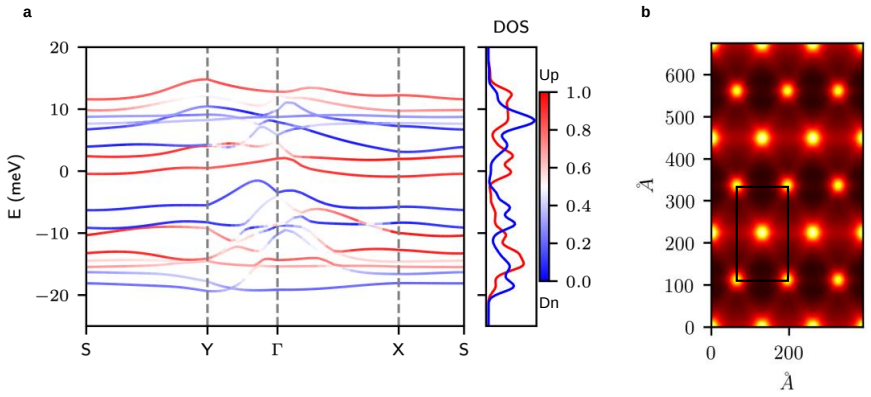

Supplementary Fig. S2. **Cosine modulation for 1D potential in the rectangular unit cell**. **a.** Bandstructure of TBG under a 1D cosine periodic potential in Eq. 2 by setting $\phi = \pi/2$, and using the same parameters $C_z = 30$ meV, $t_2 = 15$ meV, $\lambda_R = 10.5$ meV and $\Delta = 300$ meV. **b.** Colormap illustrating the cosine modulation in the rectangular unit cell using the same procedure as in the main text. The high-symmetry path in the Brillouin zone (BZ) is the same as in the manuscript.

D. Role of the different Hamiltonian terms

In Figs. S3, S4, and S5, we revisit the band-structure shown in the manuscript main text consisting of a rectangular unit cell and sine 1D modulation potential to illustrate the effect of the different terms in our Hamiltonian in more detail. In

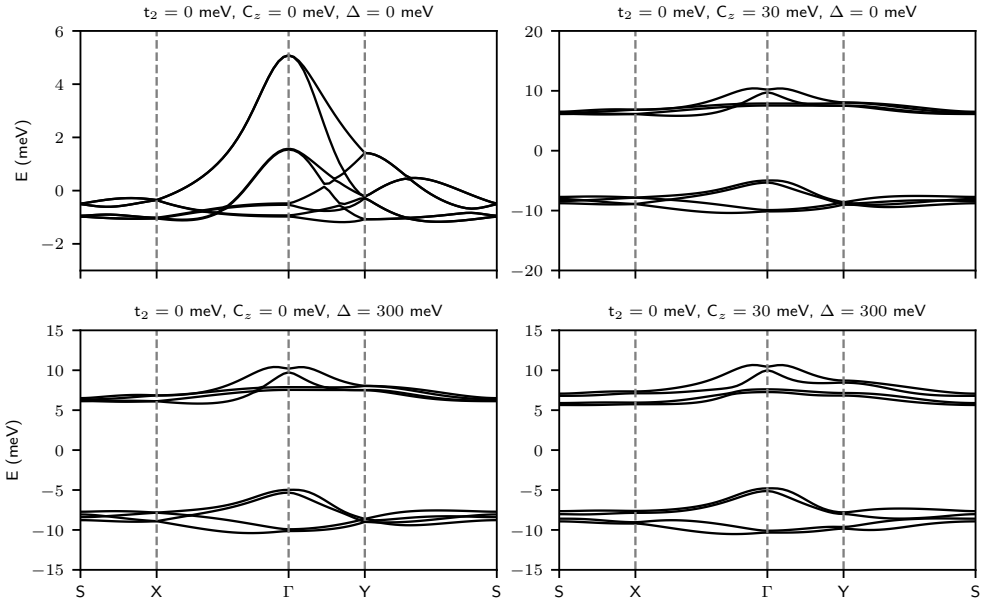

Supplementary Fig. S3. **Impact of the different Hamiltonian terms**. We gradually include the different terms from the Hamiltonian in Eq. 2 from the manuscript, while ignoring the Kane-Mele term by setting $t_2 = 0$ as well as the Rashba term by setting $\lambda_R = 0$ meV. Comparison of these figures with the final band structure in the manuscript illustrates that each term of this heuristic Hamiltonian can play an important role.

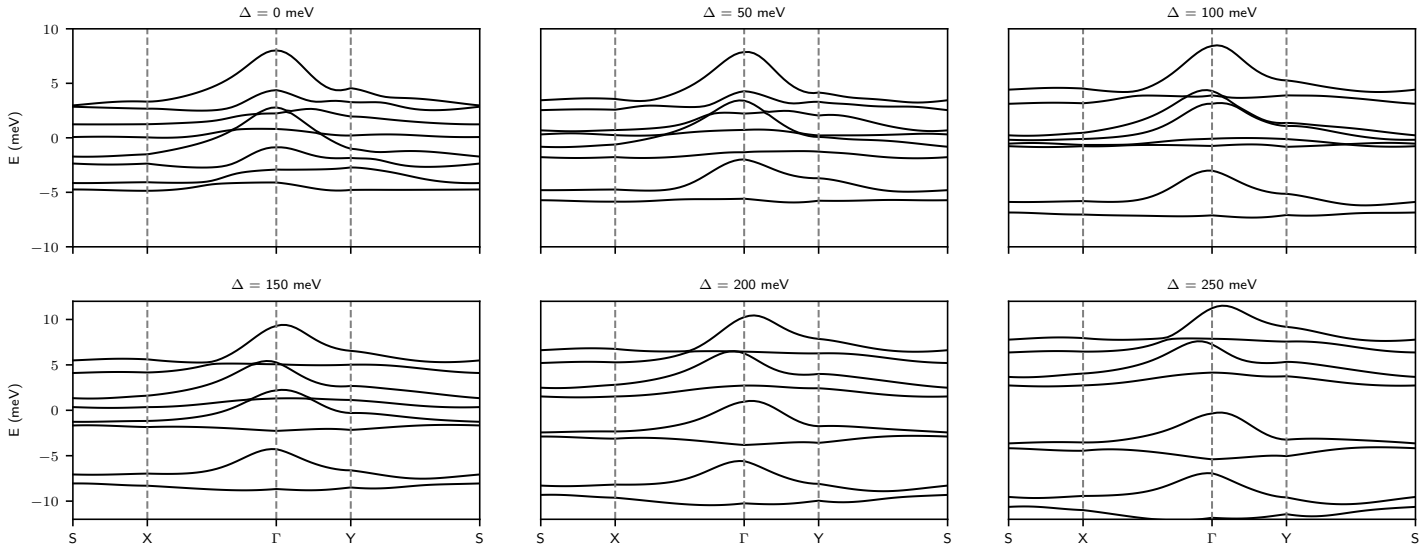

Supplementary Fig. S4. **Effect of the constant mass-term in the band separation**. We gradually increase the constant mass-term, with $t_2 = 3$ meV and $\lambda_R = 0$ meV, we only show the spin up contribution here, and $C_z = 0.03$ meV in Eq. 2 from manuscript. The constant mass term clearly increases the separation between the conduction and valence band groups that is expected to reduce interband screening and therefore enhance the chances of opening a band gap due to Coulomb interactions when the subbands are completely filled.

Fig. S3, we divide in different panels the band structures and start by showing in Fig. S3a the band structure for the TBG, nearly flat bands in the rectangular unit cell. The area of this rectangular unit cell is twice as large as the area of the single TBG system (smallest parallelogram delimited by 4 AA-stacking regions); hence we observe a doubling in the number of the flat bands. In the absence of spin, but including the valley degeneracy (inherent to our real-space approach), we have 8 flat bands in the system, distributed evenly among conduction and valence bands. In Fig. S3b, we include the 1D sine modulation pattern and observe a clear energy separation of the conduction and valence bands. Alternatively, in Fig. S3c, we check the effect of adding a constant mass-term in the bottom graphene layer using the rectangular unit cell in the absence of a sine modulation. We see that in this case, the conduction bands and valence bands are being separated from each other too, but for our choice for the value of Δ, the doubled conduction bands remain very close to each other and cannot be disentangled at the meV energy level (same observation for the doubled valence bands). We finally combine in Fig. S3d the effect of both the sine potential and the constant mass-term. The 4 valence and 4 conduction bands get separated into 2 sets of 2

bands each. We note that the weak band degeneracy lifting at the high symmetry points originates in the ξ_{c_i} factor, which differentiates between sublattices that we have included in our 1D sine modulation. We have checked that in the absence of this factor, this degeneracy lifting is nonexistent. Finally, for the case in Fig. S3d, only the Rashba and the Kane-Mele term are missing when compared to the band structure from the paper; this shows that for this choice of parameters, these terms are crucial in their ability to resolve the degeneracy lifted spins that are causing the features at $\nu = 0.5$ and 3.5. In Fig. S4, we further discuss qualitatively the effect of either the mass-term in the presence of a constant Kane-Mele term, and in Fig. S5, we vary the magnitude of the Kane-Mele term that can arise due to proximity effects induced by the substrate. We omit the Rashba term for simplicity here and only show the spin-up component. We notice that while the mass-term tends to push the highest set of valence bands above the lowest set of the conduction band, the Kane-Mele term shifts them in the opposite directions. The combination of these two terms recovers the original ordering of the bands, and both terms tend to widen the energy spectrum range where the nearly flat bands distribute.

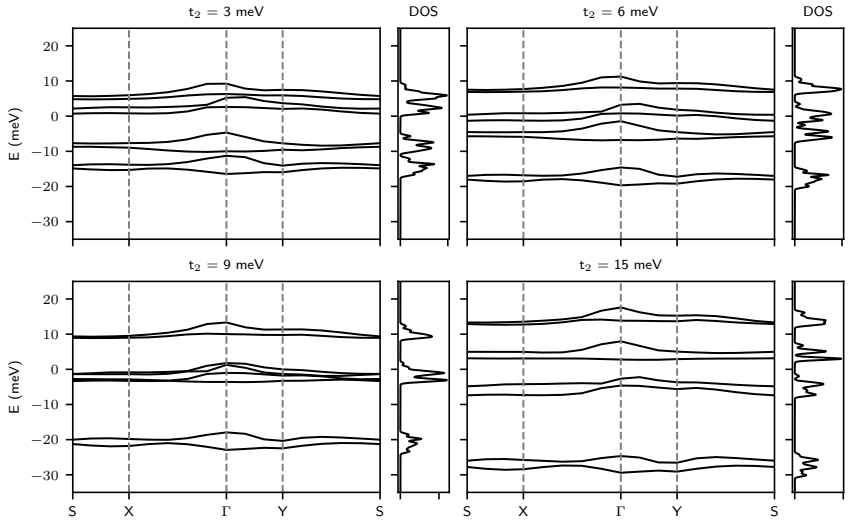

Supplementary Fig. S5. **Effect of the the value of t_2 controlling the strength of the Kane-Mele term.** We gradually increase the value of the Haldane pre-factor t_2 entering the Kane-Mele term, with $C_z = 30$ eV, $\Delta = 300$ meV and $\lambda_R = 0$ eV, in Eq. 2 from manuscript (we only show the spin-up component). Increasing the value of t_2 resolves the degeneracy of the spin-up and spin-down bands in momentum space although it does not lead to an overall splitting in the DOS.

II. EXPERIMENTAL RESULTS

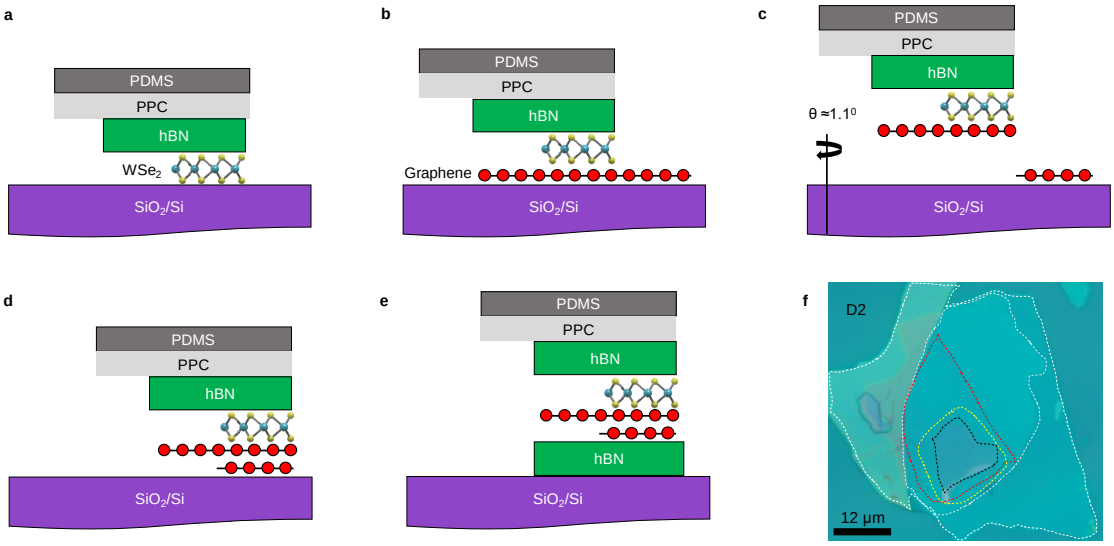

Supplementary Fig. S6. **Device fabrication**. **a-e.** Schematic of the various steps in the 'tear and stack' method used for fabrication of the moiré heterostructure. A layer of PDMS/PPC on a glass slide is used to sequentially pick the various heterostructure layers. A twist angle of $\approx 1.1^\circ$ is used to create the magic-angle twisted bilayer graphene. **f.** Optical image of the final stack for device D2. The top and bottom graphene (red and yellow), WSe_2 (black) and two hBN (white) layers are shown using dashed lines. The scale bar is 12 μm.

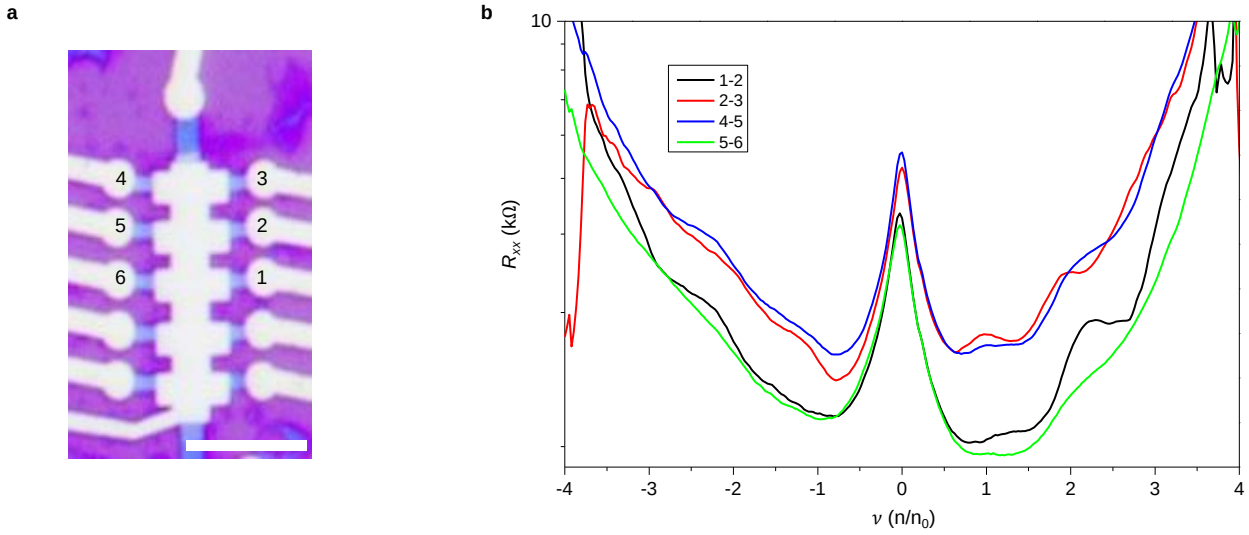

Supplementary Fig. S7. **Characterization of device D2**. **a.** Optical image of device D2 where the scalebar denotes 6 μm. **b.** Four-probe resistance measurements at $T = 6$ K for different pair of contacts show twist angle uniformity throughout the TBG/WSe_2 channel. Different colors have been used for different pairs of voltage probes. Cr/Au top gate (see (a)) was used to tune the carrier density in the Hallbar.

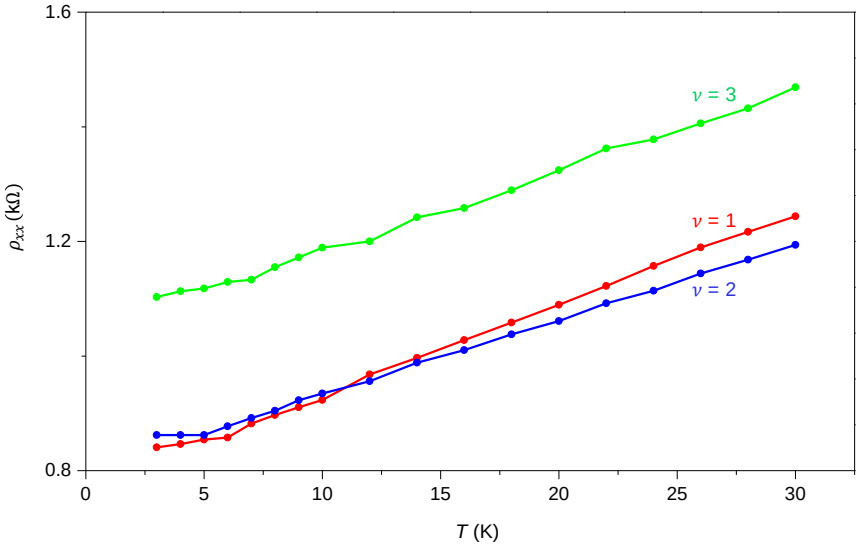

Supplementary Fig. S8. **Linear-in-T resistance in device D1,** $\theta \approx 1.14^\circ$ The longitudinal resistivity ρ_{xx} at various filling factors $\nu = 1, 2$ and 3 vary linearly with T in the measured range of temperature (3 - 30 K). The slopes for $\nu = 1$, 2, and 3 were found to be 16, 13, and 14 Ω/K respectively.

[1] Leconte, N., Javvaji, S., An, J. & Jung, J. Relaxation effects in twisted bilayer graphene: a multi-scale approach (2019). arXiv:1910.12805.
[2] Trambly de Laissardière, G., Mayou, D. & Magaud, L. Numerical studies of confined states in rotated bilayers of graphene. *Phys. Rev. B* **86**, 125413 (2012).
[3] Moon, P. & Koshino, M. Energy spectrum and quantum hall effect in twisted bilayer graphene. *Phys. Rev. B* **85**, 195458 (2012).
[4] Jung, J. & MacDonald, A. H. Tight-binding model for graphene pi-bands from maximally localized wannier functions. *Phys. Rev. B* **87**, 195450 (2013).
[5] Fast parallel algorithms for short-range molecular dynamics. *Journal of Computational Physics* **117**, 1–19 (1995).
[6] Leconte, N., Jung, J., Lebègue, S. & Gould, T. Moiré-pattern interlayer potentials in van der waals materials in the random-phase approximation. *Phys. Rev. B* **96**, 195431 (2017).